



Elastoinertial turbulence: data-driven reduced-order model based on manifold dynamics

Manish Kumar¹ , C. Ricardo Constante-Amores^{1,2}  and Michael D. Graham¹ 

¹Department of Chemical and Biological Engineering, University of Wisconsin-Madison, 1415 Engineering Dr, Madison, WI 53706, USA

²Department of Mechanical Science and Engineering, University of Illinois, Urbana-Champaign, IL 61801, USA

Corresponding author: Michael D. Graham, mdgraham@wisc.edu

(Received 4 October 2024; revised 7 December 2024; accepted 19 January 2025)

Elastoinertial turbulence (EIT) is a chaotic state that emerges in the flows of dilute polymer solutions. Direct numerical simulation (DNS) of EIT is highly computationally expensive due to the need to resolve the multiscale nature of the system. While DNS of two-dimensional (2-D) EIT typically requires $O(10^6)$ degrees of freedom, we demonstrate here that a data-driven modelling framework allows for the construction of an accurate model with 50 degrees of freedom. We achieve a low-dimensional representation of the full state by first applying a viscoelastic variant of proper orthogonal decomposition to DNS results, and then using an autoencoder. The dynamics of this low-dimensional representation is learned using the neural ordinary differential equation (NODE) method, which approximates the vector field for the reduced dynamics as a neural network. The resulting low-dimensional data-driven model effectively captures short-time dynamics over the span of one correlation time, as well as long-time dynamics, particularly the self-similar, nested travelling wave structure of 2-D EIT in the parameter range considered.

Key words: machine learning, viscoelasticity

1. Introduction

Elastoinertial turbulence (EIT) is a chaotic state resulting from the interplay between inertia and elasticity, and is suspected to set a limit on the achievable drag reduction in

turbulent flows using polymer additives (Samanta *et al.* 2013; Shekar *et al.* 2019). Direct numerical simulation (DNS) of EIT is computationally demanding due to the requirement of resolving small-scale dynamics, which is essential to sustain EIT (Sid *et al.* 2018). The dynamics of EIT is fundamentally two-dimensional (2-D) (Sid *et al.* 2018) and a 2-D numerical simulation of EIT requires $O(10^6)$ degrees of freedom (DOF), making the investigation of its dynamics challenging. A reduced-order model (ROM) of EIT having fewer DOF not only would accelerate the investigation of the dynamics of EIT but also may open the door to developing control strategies to suppress EIT, which would allow turbulent drag reduction beyond the maximum drag reduction (MDR) limit (Linot *et al.* 2023*b*). It is also of fundamental interest for any complex flow phenomenon to know how many DOF are actually required to describe its dynamics. Specifically, we have recently shown that the dynamics of 2-D EIT in channel flow is dominated by a self-similar family of well-structured travelling waves (Kumar & Graham 2024), and a natural question is how many DOF are required to capture this structure.

In this study, we use data-driven modelling techniques for the time evolution of 2-D channel flow EIT. We begin by considering the full-state data \mathbf{q} , which resides in the ambient space \mathbb{R}^{d_N} and evolves over time according to $d\mathbf{q}/dt = \mathbf{f}(\mathbf{q})$, where the mesh resolution and the number of state variables determine the size of d_N . The foundation of the data-driven reduced-order modelling approach applied here is that the long-time dynamics of a dissipative system collapse onto a relatively low-dimensional invariant manifold (Hopf 1948; Foias *et al.* 1988; Temam 1989). By mapping \mathbf{q} to invariant manifold coordinates $\mathbf{h} \in \mathbb{R}^{d_h}$ (manifold dimension $d_h < d_N$), we can describe the evolution of \mathbf{h} with a new equation $d\mathbf{h}/dt = \mathbf{g}(\mathbf{h})$ in these manifold coordinates.

A classical approach to dimension reduction is principal component analysis (PCA) (also known as proper orthogonal decomposition or POD in fluid dynamics) (Holmes *et al.* 2012). However, PCA projects data onto a flat manifold because it is an inherently linear technique, and thus may not adequately represent the generally non-flat invariant manifold where data from a complex nonlinear system lies. To capture nonlinear manifold structure, autoencoders are widely used (Kramer 1991; Milano & Koumoutsakos 2002; Linot & Graham 2020), which is the approach we pursue here. In high-dimensional systems, it can be beneficial to first apply PCA for linear dimension reduction, followed by using an autoencoder for further reduction (Linot & Graham 2023; Young *et al.* 2023; Constante-Amores *et al.* 2024). Once a low-dimensional representation of the full system state is identified, we can proceed with data-driven modelling of the dynamics to find \mathbf{g} . We use the framework, known as ‘neural ordinary differential equations (NODEs)’ (Chen *et al.* 2018; Linot & Graham 2022) that represents the vector field \mathbf{g} as a neural network. It is important to note that the Markovian nature and continuous-time framework inherent to NODEs are well-aligned with the underlying physics of the nonlinear turbulent dynamics. This framework, which we denote DManD (data-driven manifold dynamics), has been applied successfully to a wide variety of nonlinear turbulent dynamics, including Kolmogorov flow, plane Couette flow and pipe flow (Pérez-De-Jesús & Graham 2023; Linot & Graham 2023; Constante-Amores *et al.* 2024; Constante-Amores & Graham 2024). The DManD models have proven capable of accurately tracking short-term dynamics for at least one Lyapunov time and capturing key statistics of long-term trajectories, such as Reynolds stresses and energy balance in wall-bounded flows. Additionally, these models have been used to aid the discovery of new exact coherent structures (ECSs), where the ECSs are direct solutions of the governing equations and they have well-defined structures that organize dynamics in chaotic flows (e.g. travelling waves, periodic orbits) (Linot & Graham 2023; Constante-Amores *et al.* 2024).

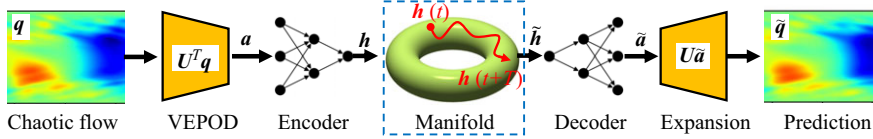


Figure 1. Framework of VEDManD used to develop a ROM of EIT.

In this study, we develop a data-driven model of EIT in 2-D channel flow. We introduce the viscoelastic data-driven manifold dynamics (VEDManD) framework, which enables the construction of low-dimensional models that faithfully capture the short-time tracking and long-time statistics in the present case using only 50 DOF (figure 1). The remainder of this article is organized as follows: § 2 outlines the methodological framework, § 3 discusses the results and § 4 concludes with final remarks.

2. Formulation and governing equations

2.1. Direct numerical simulation of EIT

The dimensionless momentum and incompressible mass conservation equations are

$$\frac{\partial \mathbf{u}}{\partial t} + \mathbf{u} \cdot \nabla \mathbf{u} = -\nabla p + \frac{\beta}{Re} \nabla^2 \mathbf{u} + \frac{1-\beta}{Re} \nabla \cdot \boldsymbol{\tau}_p + f(t) \mathbf{e}_x, \quad \nabla \cdot \mathbf{u} = 0, \quad (2.1)$$

where the non-dimensional velocity and pressure fields are denoted by \mathbf{u} and p , respectively. The unit vector along the streamwise direction is denoted \mathbf{e}_x . Lengths and velocities are made non-dimensional using the channel half-width (H) and the Newtonian laminar centreline velocity (U_c), respectively. The Reynolds number $Re = \rho U_c H / \eta$, where ρ and η are fluid density and total zero-shear rate viscosity. The solvent viscosity is η_s and $\beta = \eta_s / \eta$. The polymer stress tensor $\boldsymbol{\tau}_p$ is modelled with the finitely extensible nonlinear elastic with Peterlin closure (FEN-P) dumbbell constitutive equation:

$$\frac{\partial \boldsymbol{\alpha}}{\partial t} + \mathbf{u} \cdot \nabla \boldsymbol{\alpha} - \boldsymbol{\alpha} \cdot \nabla \mathbf{u} - (\boldsymbol{\alpha} \cdot \nabla \mathbf{u})^T = -\boldsymbol{\tau}_p + \frac{1}{ReSc} \nabla^2 \boldsymbol{\alpha}, \quad (2.2)$$

$$\boldsymbol{\tau}_p = \frac{1}{Wi} \left(\frac{\boldsymbol{\alpha}}{1 - \text{tr}(\boldsymbol{\alpha})/b} - \mathbf{I} \right), \quad (2.3)$$

where $\boldsymbol{\alpha}$ is the conformation tensor, b is the maximum extensibility of the polymer chains and \mathbf{I} is the identity tensor. The Weissenberg number $Wi = \lambda U_c / H$, where λ is the polymer relaxation time. To ensure numerical stability, we include a small diffusion term in the evolution equation of the conformation tensor (2.2), whose strength is controlled by the Schmidt number $Sc = \eta / (\rho D)$, where D is the diffusion coefficient of the polymer molecules.

We solve the governing equations in 2-D channel flow using no-slip boundary conditions at the channel walls, $y = \pm 1$. The introduction of diffusion requires boundary conditions for $\boldsymbol{\alpha}$ to evolve (2.2). As has been done elsewhere (e.g. Sid *et al.* 2018), at the walls, we solve (2.2) with no diffusion term (i.e. $1/Sc = 0$) and use the solution as the boundary condition on $\boldsymbol{\alpha}$ for (2.2) with finite Sc . We impose periodic boundary conditions in the flow (x) direction. An external force in the streamwise direction ($f(t) \mathbf{e}_x$) drives the flow. This forcing is chosen at each time step to ensure that the volumetric flow rate remains at the Newtonian laminar value.

Direct numerical simulations are performed using Dedalus (Burns *et al.* 2020), an open-source tool based on the spectral method. The channel has a length of 5 units and a

height of 2 units, and the computational domain is discretized using 256 Fourier and 1024 Chebyshev basis functions with 3/2 dealiasing factor in the streamwise (x) and wall-normal (y) directions, respectively. We consider a dilute polymer solution ($\beta = 0.97$) of long polymer chains ($b = 6400$) at $Re = 3000$, $Wi = 35$. For polymer additives, such as polyethylene oxide and polyacrylamide, this value of b corresponds to molecular weights ~ 300 kDa and ~ 500 kDa, respectively. The Schmidt number is $Sc = 250$, consistent with previous studies (Sid *et al.* 2018; Kumar & Graham 2024).

2.2. Linear dimension reduction: viscoelastic proper orthogonal decomposition

Due to the very high dimension of the EIT data ($\approx 1.6 \times 10^6$), it is desirable to begin the dimension reduction process with a linear step to reduce to a smaller (but still fairly large) dimension at which the subsequent nonlinear step will be more tractable (figure 1). To do so, we use a viscoelastic variant (Wang *et al.* 2014) of POD (Holmes *et al.* 2012), which we will denote ‘VEPOD’. The aim of VEPOD is to find a function $\psi(\mathbf{x})$ that maximizes the objective function

$$E\{|\langle \mathbf{q}(\mathbf{x}), \psi(\mathbf{x}) \rangle|^2\} \tag{2.4}$$

given the constraint $\langle \psi(\mathbf{x}), \psi(\mathbf{x}) \rangle = 1$, where \mathbf{x} denotes the position and $\langle \cdot, \cdot \rangle$ represents an inner product (further discussed below). The expectation and modulus operations over the ensemble of data are given by $E\{\cdot\}$ and $|\cdot|$, respectively. Here, $\mathbf{q}(\mathbf{x})$ is a vector containing instantaneous state variables and the ensemble we average over is a long time series.

An appropriate inner product for VEPOD can be found by considering the total mechanical energy of the fluid, which consists of the kinetic energy contribution (U_k) from the velocity and the elastic energy contribution (U_e) from the stretching of the polymer chains. For the FENE-P model, precisely computing the mechanical energy is challenging because of the limitations introduced by Peterlin’s approximation. However, an approximate mechanical energy can be given as

$$U_{tot} = U_k + U_e = \frac{1}{2} \int_{\Omega} \left\{ \mathbf{u} \cdot \mathbf{u} + \frac{1 - \beta}{ReWi} \boldsymbol{\theta} : \boldsymbol{\theta} \right\} dx, \tag{2.5}$$

where $\boldsymbol{\theta} \cdot \boldsymbol{\theta} = \boldsymbol{\alpha} / (1 - (tr(\boldsymbol{\alpha})/b))$ (Wang *et al.* 2014) and Ω denotes domain volume. For the Oldroyd-B model ($b \rightarrow \infty$), (2.5) represents the exact mechanical energy. Corresponding to this energy definition, an appropriate state variable $\mathbf{q}(\mathbf{x})$ is

$$\mathbf{q} = [\mathbf{u}, \mathbf{T}], \tag{2.6}$$

where $\mathbf{T} = \sqrt{(1 - \beta)/(ReWi)} \boldsymbol{\theta}$ is the weighted symmetric square root of the conformation tensor, which we call the stretch tensor. Consequently, the inner product used in (2.4) can be defined as

$$\langle \mathbf{q}, \psi \rangle = \int_{\Omega} \mathbf{q}(\mathbf{x}) \cdot \psi(\mathbf{x}) dx, \tag{2.7}$$

so that the inner product of \mathbf{q} with itself yields $2U_{tot}$. Maximization of the objective function (2.4) gives a self-adjoint eigenvalue problem:

$$\int_{\Omega} E\{\mathbf{q}(\mathbf{x}) \mathbf{q}^*(\mathbf{y})\} \psi(\mathbf{y}) dy = \sigma \psi(\mathbf{x}), \tag{2.8}$$

which leads to an infinite set of eigenmodes $\{\sigma_j, \psi_j(\mathbf{x})\}$ arranged in decreasing value of the energy represented by the eigenvalue σ_j . The eigenfunctions $\psi_j(\mathbf{x})$ are orthonormal

with the given inner product. The vector of VEPOD coefficients \mathbf{a} is given by $a_j = \langle \mathbf{q}(\mathbf{x}), \boldsymbol{\psi}_j(\mathbf{x}) \rangle$. The state variables can be reconstructed using VEPOD modes as

$$\tilde{\mathbf{q}}(\mathbf{x}) = \sum_{j=1}^{d_a} a_j \boldsymbol{\psi}_j(\mathbf{x}), \quad (2.9)$$

where d_a represents the number of VEPOD modes used in the reconstruction. To estimate the VEPOD of a discrete dataset, we arrange the snapshots of the flow state as

$$\mathbf{Q} = [\mathbf{q}_1, \mathbf{q}_2, \dots, \mathbf{q}_{N_t}], \quad (2.10)$$

where $\mathbf{q}_i = \mathbf{q}(t_i)$ and N_t represents the total number of snapshots. The eigenmodes of VEPOD can be obtained by solving the following discretized eigenvalue problem:

$$\mathbf{Q}\mathbf{Q}^* \mathbf{W}\boldsymbol{\psi} = \boldsymbol{\psi}\boldsymbol{\sigma}, \quad (2.11)$$

where $\boldsymbol{\sigma}$ is a diagonal matrix containing the eigenvalues, and \mathbf{W} accounts for the numerical quadrature necessary for integration on a non-uniform grid.

2.3. Non-linear dimension reduction and NODE

After projecting the data to the leading VEPOD modes, we perform a nonlinear dimension reduction with a ‘hybrid autoencoder’ (Linot & Graham 2020) to determine the mapping into the manifold coordinates $\mathbf{h} = \boldsymbol{\chi}(\mathbf{a})$, along with mapping back $\tilde{\mathbf{a}} = \check{\boldsymbol{\chi}}(\mathbf{h})$. This hybrid autoencoder uses two neural networks to learn the corrections from the leading VEPOD coefficients, as $\mathbf{h} = \boldsymbol{\chi}(\mathbf{a}; \theta_{\mathcal{E}}) = \mathbf{U}_{d_h}^T \mathbf{a} + \mathcal{E}(\mathbf{U}_{d_a}^T \mathbf{a}, \theta_{\mathcal{E}})$, here $\mathbf{U}_k \in \mathbb{R}^{d_N \times k}$ is a matrix whose columns are the first k VEPOD eigenfunctions, and \mathcal{E} is an encoding neural network having weights $\theta_{\mathcal{E}}$. The mapping back to the full space is given by $\tilde{\mathbf{a}} = \check{\boldsymbol{\chi}}(\mathbf{h}; \theta_{\mathcal{D}}) = \mathbf{U}_{d_a} [\mathbf{h}, 0]^T + \mathcal{D}(\mathbf{h}; \theta_{\mathcal{D}})$, where \mathcal{D} is a decoding neural network having weights $\theta_{\mathcal{D}}$. The autoencoder minimizes the error

$$\mathcal{L} = \|\mathbf{a}(t_i) - \check{\boldsymbol{\chi}}(\boldsymbol{\chi}(\mathbf{a}(t_i)); \theta_{\mathcal{E}}); \theta_{\mathcal{D}})\|^2 + \kappa \|\mathcal{E}(\mathbf{U}_{d_a}^T \mathbf{a}(t_i); \theta_{\mathcal{E}}) + \mathcal{D}_{d_h}(\mathbf{h}(t_i); \theta_{\mathcal{D}})\|^2, \quad (2.12)$$

where the second term is a penalty to enhance the accurate representation of the leading d_h VEPOD coefficients (Linot & Graham 2020) (in this study, $\kappa = 1$).

Once the low-dimensional representation of the full state is discovered, we use a ‘stabilized’ NODE to learn the dynamics in manifold coordinates, i.e. $d\mathbf{h}/dt = \mathbf{g}(\mathbf{h}) - \mathbf{A}\mathbf{h}$, where \mathbf{g} is a neural network, and $\mathbf{A} = \gamma \mathbf{I}S(\mathbf{h})$ is a diagonal matrix, where $S(\mathbf{h})$ is the standard deviation of \mathbf{h} and γ is a tuneable parameter. This term stabilizes the system by preventing the dynamics from drifting away from the attractor (Linot *et al.* 2023a). The NODE is trained to minimize the difference between the true state $\mathbf{h}(t_i + \Delta t_s)$ and the predicted state $\tilde{\mathbf{h}}(t_i + \Delta t_s)$:

$$\mathcal{J} = \|\tilde{\mathbf{h}}(t_i + \Delta t_s) - \mathbf{h}(t_i + \Delta t_s)\|^2, \quad (2.13)$$

where $\tilde{\mathbf{h}}(t_i + \Delta t_s) = \mathbf{h}(t_i) + \int_{t_i}^{t_i + \Delta t_s} (\mathbf{g}(\mathbf{h}) - \mathbf{A}\mathbf{h}) dt$ is a time forward prediction of the NODE over time interval Δt_s . Details of the different neural networks are summarized in table 1.

The ROM of EIT in the present study has been developed using a statistically stationary dataset consisting of 1000 time units simulated using time step $\Delta t = 0.001$ and sampled at the interval of $\Delta t_s = 0.025$ time units, which leads to a total of 40 000 snapshots. The correlation time of the dynamics of EIT is small (< 1 time unit), so this dataset is sufficient to develop our ROM. Here, 80 % of data have been used for training and 20 % data for

Neural Network	Architecture	Activation	Learning rate
Encoder (\mathcal{E})	4000 : 5000 : 1000 : 250 : d_h	ReLU:ReLU:ReLU:Lin	$[4 \times 10^{-4}, 10^{-4}]$
Decoder (\mathcal{D})	d_h : 250 : 1000 : 5000 : 4000	ReLU:ReLU:ReLU:Lin	$[4 \times 10^{-4}, 10^{-4}]$
NODE (\mathcal{g})	d_h : 500 : 500 : d_h	Sig:Sig:Lin	$[10^{-4}, 10^{-5}]$

Table 1. Details of different neural networks used in the VEDManD framework. ‘Architecture’ represents the dimension of each layer and ‘Activation’ refers to the types of activation functions used, where ‘ReLU’, ‘Sig’ and ‘Lin’ stand for Rectified Linear Unit, Sigmoid and Linear activation functions, respectively. ‘Learning Rate’ represents the learning rates used during training.

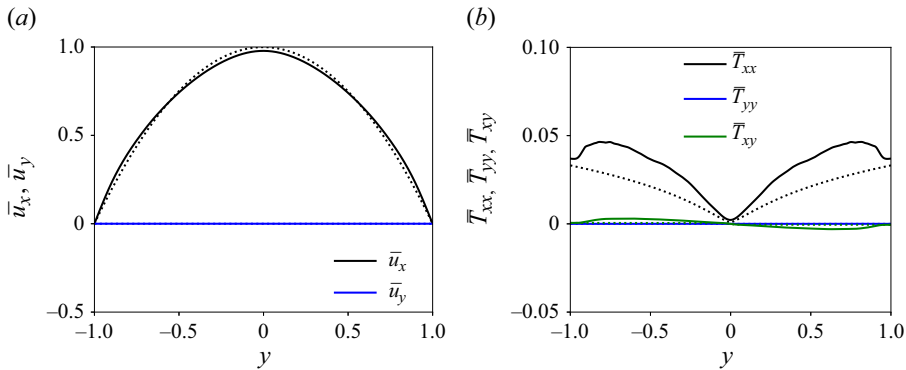


Figure 2. Mean profiles (solid lines) of the components of (a) velocity and (b) stretch tensor in EIT at $Re = 3000$ and $Wi = 35$. The dotted lines show the laminar profiles at the same parameter. The temporal mean profiles of velocity in EIT are close to the laminar profiles as velocity fluctuations in EIT are weak (Sid *et al.* 2018).

testing. The losses used to train the neural networks (2.12) and (2.13) are the ensemble-averaged over the training data. The DNS was performed in parallel mode on 24 processors on a high-performance computing (HPC) cluster and it took ≈ 2 weeks to compute for 1000 time units. The VEDManD framework consists of three steps, and a single processor was used to develop our ROM. The first step, the projection of the dataset on 4000 VEPOD modes, takes ≈ 4 hours. The second step, the training of the autoencoder, takes ≈ 2 days. The third step, the training of the NODE, takes 2–3 hours. Thus, the development of ROM takes ≈ 2.5 days on a single processor. Once the model is developed, it evolves dynamics for 1000 time units in seconds on a single processor.

3. Results and discussion

3.1. Dimension reduction of EIT

For statistically stationary dynamics, the instantaneous state variables can be written as $\mathbf{u} = \bar{\mathbf{u}} + \mathbf{u}'$ and $\mathbf{T} = \bar{\mathbf{T}} + \mathbf{T}'$, where $\bar{(\cdot)}$ and $(\cdot)'$ are the temporal mean and perturbation, respectively. Mean profiles and laminar profiles are shown in figures 2(a) and 2(b), respectively. Here, we develop a ROM to capture the perturbations of the state variables: $\mathbf{q} = [\mathbf{u}', \mathbf{T}']$.

The VEPOD eigenvalue spectrum of the perturbations in state variables, figure 3(a), shows that the energy content of higher VEPOD modes decreases approximately exponentially for index $j \gtrsim 1500$. We find that reconstruction of the flow state using

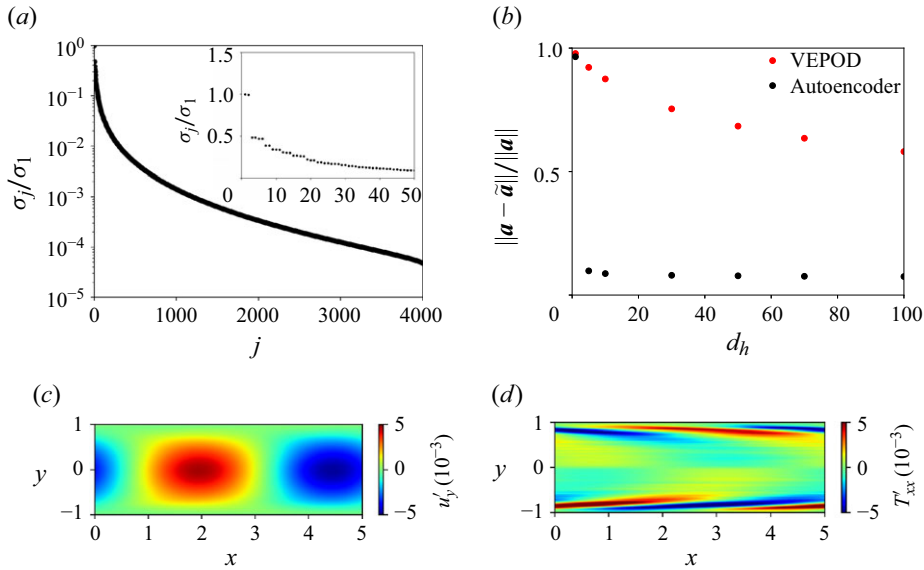


Figure 3. (a) The VEPOD eigenvalue spectrum. (b) Normalized reconstruction error on the test dataset for various latent dimensions of VEPOD and autoencoder. Leading VEPOD mode structure for (c) u'_y and (d) T'_{xx} .

$d_a = 4000$ VEPOD modes captures $\approx 99.8\%$ of the total mechanical energy and yields an accurate representation. Therefore, to develop our model we retain 4000 VEPOD modes. We also visualize the leading VEPOD mode structure for u'_y and T'_{xx} (figure 3c,d) and find that they resemble the most dominant travelling wave underlying EIT (Kumar & Graham 2024).

Before training the neural networks, we first centre and scale the dataset by subtracting the mean and then normalizing it with the maximum standard deviation. To find a low-dimensional representation of the system, we train multiple autoencoders with varying numbers of latent dimensions and visualize the reconstruction error of VEPOD coefficients on the test dataset (figure 3b). The reconstruction error initially decreases rapidly at low d_h , then shows only a marginal improvement in the reconstruction for latent dimension $d_h > 30$. The VEDManD model with $d_h = 30$ struggles to quantitatively capture the dynamics, so we do not report results for it and we use the latent dimension of the autoencoder $d_h = 50$ in the present study. To illustrate the accuracy of the reconstruction, we compare results for u'_y and T'_{xx} fields using the autoencoder at $d_h = 50$ (figure 4c,d) with the corresponding DNS results (figure 4a,b). The autoencoder faithfully reconstructs the flow state obtained from the DNS. Visual inspection of the autoencoder reconstruction reveals a very close resemblance, while a quantitative comparison between DNS and autoencoder results demonstrates differences at fine scales in the reconstruction ($\sim 10\%$ for the worst-case scenario and are confined only in a tiny region), resulting from the cumulative effects of VEPOD truncation and autoencoder reconstruction (figure 4e,f). Further analysis shows that the error is dominated by VEPOD truncation to 4000 modes – the autoencoder error is very small. The other components exhibit similar degrees of accuracy.

3.2. Low-dimensional dynamic model

Once the autoencoder maps the system on a low-dimensional representation, we train the NODE to predict dynamics. We start the presentation of the NODE results with

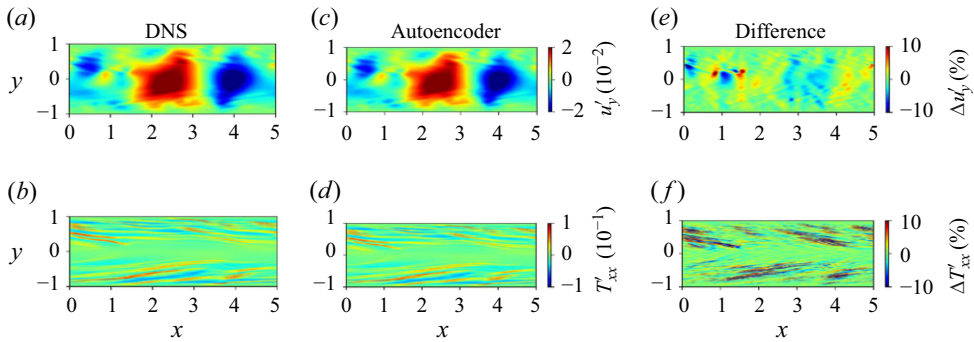


Figure 4. Instantaneous (a,c) u'_y and (b,d) T'_{xx} obtained from (a,b) DNS and (c,d) reconstruction with an autoencoder with $d_h = 50$. (e,f) Difference between DNS and autoencoder reconstruction normalized with the maximum values of respective fields.

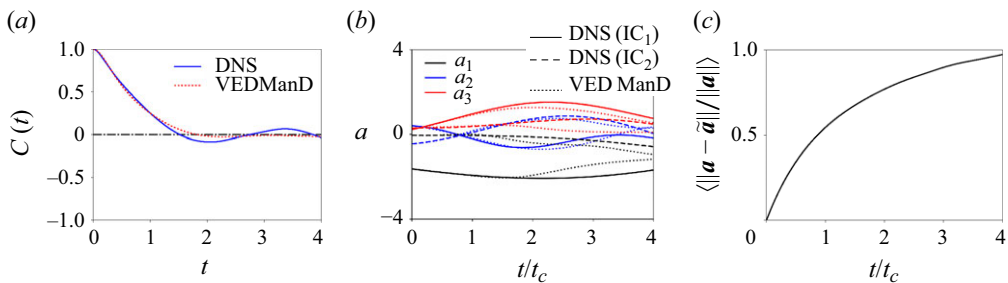


Figure 5. (a) Temporal autocorrelation of the VEPOD coefficients. (b) First several VEPOD coefficients up to $t/t_c = 4$ obtained using DNS and VEDManD with $d_h = 50$ for two arbitrary initial conditions (IC₁ and IC₂). (c) Ensemble-averaged relative error between the VEPOD coefficients obtained using DNS and VEDManD.

short-time tracking. It is expected that the VEDManD predictions should closely follow DNS trajectories over a short time period before the dynamics diverges due to the chaotic nature of the system. To estimate the correlation time of the dynamics, we defined a temporal autocorrelation function ($C(t)$) for the VEPOD coefficients as $C(t) = (\langle \mathbf{R}(\tau) \cdot \mathbf{R}(\tau + t) \rangle) / (\langle \mathbf{R}(\tau) \cdot \mathbf{R}(\tau) \rangle)$, where $\langle \cdot \rangle$ represents ensemble average. Here, the parameter \mathbf{R} stands for \mathbf{a} and $\tilde{\mathbf{a}}$ for DNS and VEDManD, respectively. The autocorrelation functions from DNS and VEDManD are plotted in figure 5(a). The correlation time of the dynamics is defined as $t_c = \int_0^{t_z} C(t) dt$, where t_z represents the first zero of the autocorrelation function. The computed values using DNS and VEDManD are $t_c = 0.67$ and $t_c = 0.68$, respectively, very close to each other. This time scale indicates when trajectories starting from different initial conditions or with slightly different evolution equations should start to diverge from one another. In figure 5(b), we show the time evolution of the first several VEPOD coefficients for different initial conditions on the attractor using the VEDManD model and DNS. For $t < t_c$, the model accurately predicts the EIT trajectory, deviating at longer times. In figure 6, we compare snapshots of the state obtained from the model against DNS with the same initial condition and see that for $t < t_c$ the results are very close. To quantify the deviation of the VEDManD prediction of trajectories from the DNS results, we show in figure 5(c) the ensemble average of the relative error of the VEPOD coefficients from VEDManD and DNS calculated over many

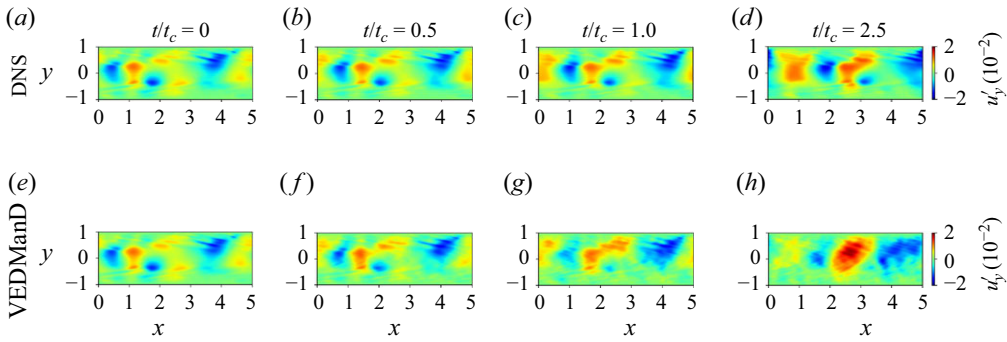


Figure 6. Time series of u'_y obtained using (a–d) DNS and (e–h) VEDManD for IC_1 in figure 5(b).

initial conditions. The difference between the model prediction and the DNS result is small at short times, increasing on the time scale t_c before saturating. In summary, the VEDManD model with $d_h = 50$ is capable of accurately capturing the dynamics of 2-D EIT over time scales comparable to the flow correlation time.

We now turn to the long-time statistics of the timeevolution, focusing on the spectral proper orthogonal decomposition (SPOD) (Towne *et al.* 2018), of the flow and stretch fields. In short, SPOD is a temporal variant of POD that seeks the frequency-by-frequency POD of a Fourier-transformed time-dependent flow, yielding for every frequency f a spectrum of energies and modes. For a detailed description of SPOD in the context of EIT, see Kumar & Graham (2024), where we used SPOD to show that the dynamics of 2-D EIT in the parameter regime examined are dominated by a family of self-similar, nested travelling waves. Here, we report the SPOD spectrum of u'_y , as this component gives the cleanest spectrum. The SPOD energy spectra of u'_y obtained from DNS and VEDManD are shown in figures 7(a) and 7(b), respectively. The leading modes of both spectra contain most of the energy and exhibit peaks at the same frequencies, at least to the two significant digits (red symbols) which is the frequency resolution in the present study. We visualize the SPOD mode structures corresponding to the peaks in the SPOD spectra in figure 8. The structures obtained from the VEDManD model closely resemble the structures of travelling modes obtained from the DNS. (The mode structures are travelling waves, therefore we align their spatial phases to make comparison easier.) The precise prediction of wavenumbers and frequencies of different mode structures by the VEDManD model gives an accurate prediction of their wave speeds. Thus, we have found a highly accurate representation of EIT with $O(10)$ dimensions commencing from an initial state dimension of $O(10^6)$. This dimension might not be the true dimension of the invariant manifold where the dynamics lives (this quantity remains difficult to estimate precisely from data for complex chaotic systems), but it is capable of providing models that faithfully capture the short-time dynamics and long-time statistics of EIT.

4. Conclusion

Numerical simulations of EIT are computationally expensive due to the high number of DOF ($O(10^6)$) required to resolve all spatial and temporal scales. In the present study, we use data-driven methods to develop a ROM that has far fewer DOF ($O(10)$) yet nevertheless captures these scales and the dynamics of EIT. To find the low-dimensional representation of the full state, we first introduce a variant of VEPOD which reduces

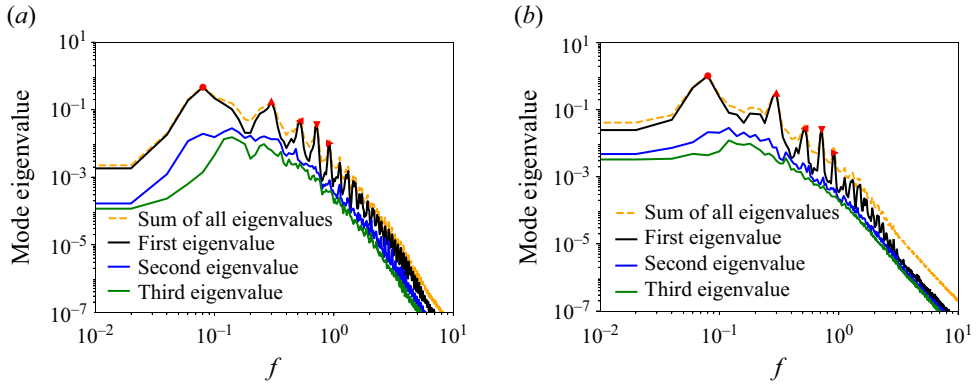


Figure 7. The SPOD eigenvalue spectra of u'_y obtained using (a) DNS and (b) VEDManD. Red symbols indicate peaks in the leading mode of the spectra.

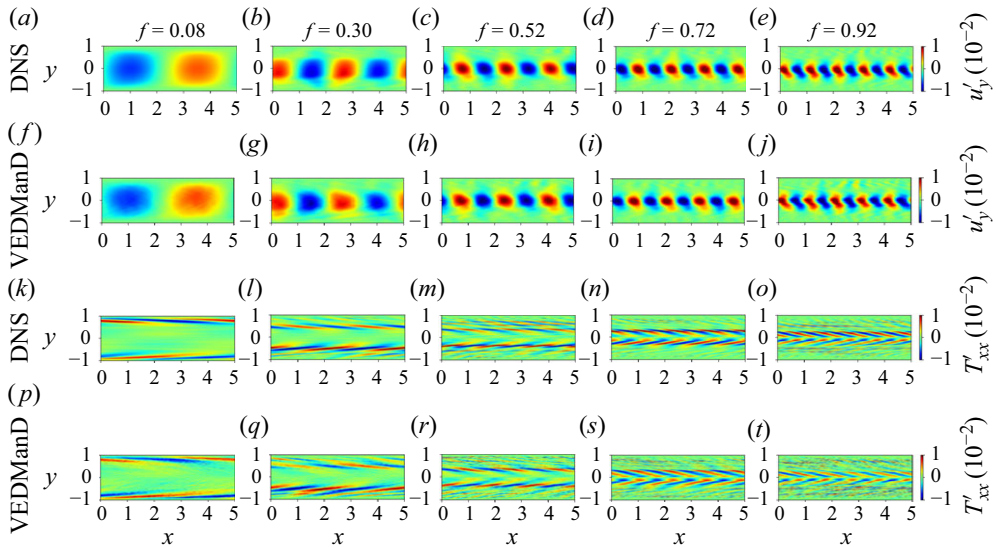


Figure 8. The SPOD mode structures of (a–j) u'_y and (k–t) T'_{xx} from (a–e, k–o) DNS and (f–j, p–t) VEDManD at the frequencies indicated with red symbols in figure 7.

the dimension of the EIT dataset from $O(10^6)$ to $O(10^3)$, and then use autoencoders to perform nonlinear dimension reduction from $O(10^3)$ to $O(10)$. To evolve dynamics on this low-dimensional representation, we use stabilized NODEs. A ROM with a dimension of 50 accurately predicts both short-time dynamics and long-time statistics. This model successfully captures the trajectory of the dynamics over the span of one correlation time. To analyse the long-time statistics of the dynamics, we use SPOD and show that the ROM accurately captures the complex nonlinear structures and the frequencies of the self-similar travelling waves that underlie the chaotic dynamics observed in the DNS of 2-D EIT.

By accurately modelling EIT with significantly fewer DOF than DNS requires, manifold dynamics models like those presented here make it possible to perform computationally efficient analyses, such as calculating Floquet multipliers and local Lyapunov exponents.

Such models can accelerate the discovery of new ECSs (e.g. periodic orbits, relative periodic orbits) underlying EIT (Linot & Graham 2023). These models could also facilitate the design of control strategies (such as patterning surfaces) using a reduced number of DOF which would allow turbulent drag reduction using polymer additives beyond the MDR limit.

Funding. This research was supported under grant ONR N 00014-18-1-2865 (Vannevar Bush Faculty Fellowship).

Declaration of interests. The authors report no conflict of interest.

REFERENCES

- BURNS, K.J., VASIL, G.M., OISHI, J.S., LECOANET, D. & BROWN, B.P. 2020 Dedalus: a flexible framework for numerical simulations with spectral methods. *Phys. Rev. Res.* **2** (2), 023068.
- CHEN, R.T.Q., RUBANOVA, Y., BETTENCOURT, J. & DUVENAUD, D.K. 2018 Neural ordinary differential equations. In *Advances in Neural Information Processing Systems* (eds. S. BENGIO, H. WALLACH, H. LAROCHELLE, K. GRAUMAN, N. CESA-BIANCHI & R. GARNETT), vol. 31, pp. 1–13. Curran Associates.
- CONSTANTE-AMORES, C.R. & GRAHAM, M.D. 2024 Data-driven state-space and Koopman operator models of coherent state dynamics on invariant manifolds. *J. Fluid Mech.* **984**, R9.
- CONSTANTE-AMORES, C.R., LINOT, A.J. & GRAHAM, M.D. 2024 Dynamics of a data-driven low-dimensional model of turbulent minimal pipe flow. [arXiv: 2408.03135](https://arxiv.org/abs/2408.03135)
- FOIAS, C., SELL, G.R. & TEMAM, R. 1988 Inertial manifolds for nonlinear evolutionary equations. *J. Differ. Equ.* **73** (2), 309–353.
- HOLMES, P., LUMLEY, J.L., BERKOOZ, G. & ROWLEY, C.W. 2012 *Turbulence, Coherent Structures, Dynamical Systems and Symmetry*. 2nd edn. Cambridge University Press.
- HOPF, E. 1948 A mathematical example displaying features of turbulence. *Commun. Pure Appl. Maths* **1** (4), 303–322.
- KRAMER, M.A. 1991 Nonlinear principal component analysis using autoassociative neural networks. *AIChE J.* **37** (2), 233–243.
- KUMAR, M. & GRAHAM, M.D. 2024 Nested travelling wave structures in elastoinertial turbulence. *J. Fluid Mech.* **993**, A8.
- LINOT, A.J., BURBY, J.W., TANG, Q., BALAPRAKASH, P., GRAHAM, M.D. & MAULIK, R. 2023a Stabilized neural ordinary differential equations for long-time forecasting of dynamical systems. *J. Comput. Phys.* **474**, 111838.
- LINOT, A.J. & GRAHAM, M.D. 2020 Deep learning to discover and predict dynamics on an inertial manifold. *Phys. Rev. E* **101** (6), 062209.
- LINOT, A.J. & GRAHAM, M.D. 2022 Data-driven reduced-order modeling of spatiotemporal chaos with neural ordinary differential equations. *Chaos* **32** (7), 073110.
- LINOT, A.J. & GRAHAM, M.D. 2023 Dynamics of a data-driven low-dimensional model of turbulent minimal Couette flow. *J. Fluid Mech.* **973**, A42.
- LINOT, A.J., ZENG, K. & GRAHAM, M.D. 2023b Turbulence control in plane Couette flow using low-dimensional neural ODE-based models and deep reinforcement learning. *Intl J. Heat Fluid Flow* **101** (January), 109139.
- MILANO, M. & KOUMOUTSAKOS, P. 2002 Neural network modeling for near wall turbulent flow. *J. Comput. Phys.* **182** (1), 1–26.
- PÉREZ-DE-JESÚS, C.E. & GRAHAM, M.D. 2023 Data-driven low-dimensional dynamic model of Kolmogorov flow. *Phys. Rev. Fluids* **8** (4), 044402.
- SAMANTA, D., DUBIEF, Y., HOLZNER, M., SCHÄFER, C., MOROZOV, A.N., WAGNER, C. & HOF, B. 2013 Elasto-inertial turbulence. *Proc. Natl Acad. Sci. USA* **110** (26), 10557–10562.
- SHEKAR, A., MCMULLEN, R.M., WANG, S., MCKEON, B.J. & GRAHAM, M.D. 2019 Critical-layer structures and mechanisms in elastoinertial turbulence. *Phys. Rev. Lett.* **122** (12), 124503.
- SID, S., TERRAPON, V.E. & DUBIEF, Y. 2018 Two-dimensional dynamics of elasto-inertial turbulence and its role in polymer drag reduction. *Phys. Rev. Fluids* **3** (1), 011301.
- TEMAM, R. 1989 Do inertial manifolds apply to turbulence? *Physica D: Nonlinear Phenom.* **37** (1-3), 146–152.
- TOWNE, A., SCHMIDT, O.T. & COLONIUS, T. 2018 Spectral proper orthogonal decomposition and its relationship to dynamic mode decomposition and resolvent analysis. *J. Fluid Mech.* **847**, 821–867.

- WANG, S., GRAHAM, M.D., HAHN, F.J. & XI, L. 2014 Time-series and extended Karhunen–Loève analysis of turbulent drag reduction in polymer solutions. *AIChE J.* **60** (4), 1460–1475.
- YOUNG, C.D., CORONA, P.T., DATTA, A., HELGESON, M.E. & GRAHAM, M.D. 2023 Scattering-informed microstructure prediction during lagrangian evolution (simple)—a data-driven framework for modeling complex fluids in flow. *Rheol. Acta* **62** (10), 587–604.